Microstructural Evolution and Behavior of Deuterium in a Ferritic ODS 12 Cr Steel Annealed at Different Temperatures

Marques Pereira, V.; Wang, S.; Morgan, T.; Schut, H.; Sietsma, J.

DOI
10.1007/s11661-021-06559-0

Publication date
2022

Document Version
Final published version

Published in
Metallurgical and Materials Transactions A: Physical Metallurgy and Materials Science

Citation (APA)
Marques Pereira, V., Wang, S., Morgan, T., Schut, H., & Sietsma, J. (2022). Microstructural Evolution and Behavior of Deuterium in a Ferritic ODS 12 Cr Steel Annealed at Different Temperatures. *Metallurgical and Materials Transactions A: Physical Metallurgy and Materials Science*, *53*(3), 874-892. https://doi.org/10.1007/s11661-021-06559-0

ORIGINAL RESEARCH ARTICLE

Microstructural Evolution and Behavior of Deuterium in a Ferritic ODS 12 Cr Steel Annealed at Different Temperatures

V.S.M. PEREIRA, S. WANG, T. MORGAN, H. SCHUT, and J. SIETSMA

In the present work, an ODS 12 Cr steel was characterized using Electron Microscopy techniques, in an as-received condition and after annealing treatments between 773 K and 1573 K. Results show a complex microstructure, with the presence of fine Y–Ti–O nanoparticles dispersed in the matrix. After annealing at 1573 K, the average diameter of Y–Ti–O nanoparticles increases from ~ 4 to ~ 7 nm and partial recrystallization occurs. The trapping behavior of deuterium in the steel in its as-received state and annealed at 1573 K was investigated. Samples were exposed to low-energy deuterium plasma and analyzed with thermal desorption spectroscopy, after waiting times of 1 day and 25 days. The samples measured 1 day after exposure released a higher total amount of deuterium than the ones measured after 25 days. The effect of waiting time is explained by the release of deuterium, at 300 K, from sites with low activation energy for detrapping, E_d. In the as-received condition, part of the deuterium detrapped at 300 K was re-trapped by high-E_d sites. For the samples in the annealed condition, the redistribution of deuterium from low-E_d to high-E_d sites was not observed, but the total amount of deuterium released was higher.

https://doi.org/10.1007/s11661-021-06559-0

I. INTRODUCTION

ODS ferritic steels have been extensively studied in the past decades due to their potential application as fuel cladding tubes in nuclear fast breeder reactors and on fusion reactor blankets. The Cr contents of 12 wt pct or higher promote resistance to corrosion, while the ODS nanoparticles are responsible for the good mechanical performance of the steels at high temperatures and for their resistance to radiation damage.[1–10]

Conventional fabrication routes of ODS ferritic steels involve mechanical alloying, consolidation by extrusion or hot isostatic pressing and further thermo-mechanical processing (cycles of cold rolling and annealing, hot rolling, hot forging).[1–3,6] The microstructure of ODS ferritic steels consolidated via extrusion is composed of large, elongated grains and nanosized grains. In addition, the material has a strong ⟨110⟩ α-fiber texture, formed during the extrusion process. The anisotropy in grain morphology and the ⟨110⟩ α-fiber texture lead to poor mechanical properties in the transverse direction.[2,9,11] In conventional steels, grain morphology and texture can be altered during the phase transformation of ferrite to austenite or during recrystallization. However, Cr-rich ODS ferritic steels cannot be austenitized and the ⟨110⟩ α-fiber texture is difficult to be removed, due to its inherent low driving force for recrystallization.[2] Recently, other fabrication routes which do not involve extrusion or hot isostatic pressing have been developed and promising results were reported.[8,9] Moghadasi *et al.*[8] produced an ODS ferritic alloy with nanometric Y_2TiO_5 particles dispersed in the matrix via a vacuum casting route, and Kumar *et al.*[9] obtained an ODS 18 Cr steel using powder forging as consolidation method. In Reference 9, the final forged product exhibited isotropic morphology and crystallography and, consequently, isotropic mechanical properties.

V.S.M. PEREIRA is with the Delft University of Technology, Radiation Science and Technology Department, Faculty of Applied Sciences, Mekelweg 15, 2629JB, Delft, The Netherlands and with the Delft University of Technology, Materials Science and Engineering Department, Faculty of Mechanical, Maritime and Materials Engineering, Delft, 2628CD, The Netherlands and also with the Dutch Institute for Fundamental Energy Research, Plasma and Materials Interaction Department, Eindhoven, 5612AJ, The Netherlands. Contact e-mail: v.marquespereira@tudelft.nl S. WANG and T. MORGAN are with the Dutch Institute for Fundamental Energy Research, Plasma and Materials Interaction Department. H. SCHUT is with the Delft University of Technology, Radiation Science and Technology Department, Faculty of Applied Sciences. J. SIETSMA is with the Delft University of Technology, Materials Science and Engineering Department, Faculty of Mechanical, Maritime and Materials Engineering.
Manuscript submitted June 21, 2021; accepted: November 22, 2021.

Published online: 04 January 2022

Regardless of the fabrication route used, an important aspect of alloy design, common to ODS ferritic steels, is the addition of titanium. During processing, the presence of Ti dissolved in the pre-alloy ferritic powder or added to the powder mixture as TiO_2 leads to complex Y–Ti–O particles with average particle size ranging from 3 to 10 nm. Depending on the processing parameters, the oxide nanoparticles can form with different stoichiometric compositions and crystal structures, like cubic $Y_2Ti_2O_7$, orthorhombic or hexagonal Y_2TiO_5, and orthorhombic $YTiO_3$.[1,4,6,8,12] Additionally, it has been reported by different authors that Y–Ti–O nanoparticles are coherent or semi-coherent with the ferritic matrix.[4,8,13] This type of coherency relation with the matrix has been correlated to the slow coarsening rate of the Y–Ti–O particles at high temperatures: the interfacial energy of a coherent or semi-coherent particle is low, resulting in a low driving force for coarsening.[8,13] The slow diffusion of Y in ferrite also contributes to the low coarsening rate. Hence, the Y–Ti–O particles remain refined at temperatures as high as 1473 to 1573 K and, consequently, the microstructural stability of the material is maintained.

The original concept behind the development of ODS steels was actually aimed at increasing the resistance of nuclear structural materials to He embrittlement, while their higher creep resistance is considered an additional benefit.[14,15] In nuclear environments, neutrons that impinge metallic structural components can react with the nuclei of lattice atoms, resulting in the transmutation of alloying elements plus formation of He or H.[16–18] The transmuted element can be radioactive and, hence, compromise the handling and recycling of the structural component at the end of its service life. However, this problem can be tackled by the use of elements in alloy design that go through faster decay of the induced radioactivity than conventional alloying elements.[19,20] In fusion reactors, the structural metallic components will also be exposed to D, T, He, and H, since they form the plasma in which fusion takes place or are the products of fusion reactions. These elements will diffuse through the metallic structure, being able to recombine and form gas molecules and, when pressure is sufficiently high, bubbles are detrimental for the integrity of the component. They can also be trapped at microstructural features of the metal or alloy, such as grain boundaries, interfaces of second-phase particles, dislocations, inclusions, and pores. Depending on morphological characteristics of these trapping sites and their distribution throughout the metallic matrix, they can become stress raisers when bound to these elements, leading to embrittlement and fracture during service, or they can be beneficial for increasing the resistance to damage.[21] Since it is not possible to prevent the formation of radiation-induced defects and the generation of He, H, D, and T in the metallic structure, the engineering of trapping sites becomes the most suitable approach to improve the resistance to this type of damage and that is how oxide nanoparticles in ODS steels can play their role. These particles can retain the diffusible elements and make them inactive in the material, preventing their recombination or agglomeration at detrimental sites, like grain boundaries (leading to intergranular fracture), regions with microstructural banding, and elongated inclusions.

However, it is still unclear how strongly the ODS particles can interact with the different diffusible elements and to what extent ODS steels perform well in nuclear environments. Malitckii *et al.*[22,23] have measured with Thermal Desorption Spectroscopy significantly higher contents of H in ODS Eurofer, in comparison to Eurofer, after electrochemical hydrogen charging[22] and exposure to hydrogen plasma.[23] In Reference 22, the authors determined H detrapping activation energies of 0.26 eV and 0.35 eV for the ODS Eurofer steel, at the respective peak temperatures of ~ 450 K and ~ 550 K, but without identifying the type of trapping defects. In contrast, Maroef *et al.*[24] determined an H detrapping activation energy of 0.73 eV for the interface of Y_2O_3 with ferrite, which does not coincide with detrapping activation energies measured in Reference 22. Regarding the isotopes of hydrogen, deuterium (D), and tritium (T), it can be considered that they behave in steels in the same way as hydrogen,[25] but a more complete characterization of their trapping sites is still missing in the literature. Ogorodnikova *et al.*[26] measured D retention in several ODS steels and Eurofer, after exposure to D_2 plasma of different energies and at different temperatures. The TDS measurements were carried out months after plasma exposure and showed that the D retention in the ODS materials was always higher than in Eurofer.[26] In a subsequent work, Ogorodnikova *et al.*[27] performed the same type of analysis in pre-damaged ODS steels and Eurofer, *i.e.*, that were irradiated with 20 MeV W ions prior to exposure to D_2 plasma. The authors[27] observed higher D retention in the pre-damaged samples that were exposed to D_2 plasma at temperatures up to 500 K, but still no details about the sites at which D is dominantly being trapped are discussed.[27]

Thus, in the present work, the behavior of deuterium in an ODS 12 Cr steel was investigated. First, the microstructure and the Y–Ti–O particles present in the steel were characterized in the as-received condition and after annealing treatments at different temperatures. In this way, potential trapping sites for D in the material were identified. Subsequently, samples of ODS 12 Cr steel in the as-received condition and annealed at 1573 K for 1 hour were exposed to low-energy D_2 plasma and analyzed with Thermal Desorption Spectroscopy, in order to study the trapping behavior of D and its interaction with Y–Ti–O nanoparticles.

II. MATERIAL AND METHODS

A. *Material*

The material was fabricated according to a traditional route used for ODS 12 Cr ferritic steels, which consisted of mechanical alloying, hot extrusion, and thermo-mechanical post-consolidation treatments.[28] Table I

Table I. Chemical Composition of the 0.3 Pct Y_2O_3-ODS 12 Cr Steel, in Weight Percentage

ODS 12 Cr										
Fe	C	Cr	W	Ti	Zn	Y	O*	Si	S	Al
85.08	0.03	12.29	1.72	0.30	0.04	0.14	0.05	0.17	0.04	0.13

The O content was not determined experimentally, instead, it was calculated assuming that all O present in the steel was in Y_2O_3.

presents the chemical composition of the steel, determined with X-ray fluorescence (heavy elements) and combustion analysis (C and S).

The material was received in a bar form, with thickness of 6 mm. Samples with dimensions of 15 × 15 × 1 mm^3 were taken from arbitrary positions along the thickness of the bar and isothermally treated in a vacuum furnace at 773 K, 1273 K, 1373 K, 1473 K, and 1573 K for 1 hour. *A priori* examination of the steel bar using Optical Microscopy showed an overall homogeneous microstructure along the thickness. All samples were cooled inside the furnace, by switching off the power supply, under exponential cooling with an average cooling rate of 0.5 K s^{-1}.

Although it is well known that steels containing Cr contents of 12 pct or higher are ferritic, dilatometry tests were carried out in a Bahr DIL805A/D to confirm that the material does not go through the α/γ phase transformation during heating. The samples were heated to 1273 K, at a heating rate of 10 K s^{-1}, with a holding time of 3 min, and cooled down to room temperature at different cooling rates, varying from 0.25 K s^{-1} to 60 K s^{-1}. Figure 1 contains a representative dilatometry curve, which does not present any inflection characteristic of phase transitions, confirming that the steel is fully ferritic throughout the heat treatments.

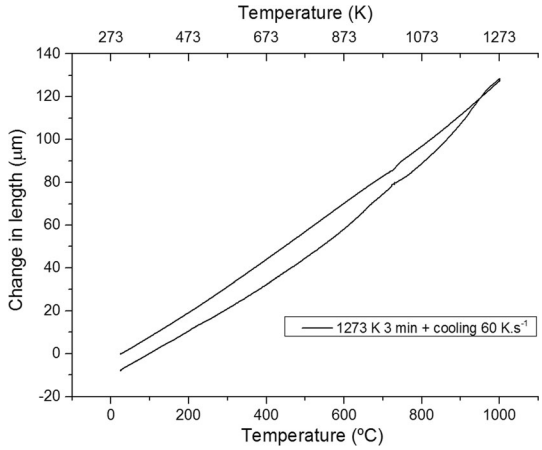

Fig. 1—Representative dilatometry curve obtained for the ODS 12 Cr after heating until 1273 K at a rate of 10 K s^{-1}, holding time of 3 min, and cooling to room temperature at 60 K s^{-1}.

B. *Methods*

1. *Characterization of the Microstructure and of Oxide Nanoparticles*

The microstructures of the as-received and annealed conditions were characterized with scanning electron microscopy (SEM), energy-dispersive X-ray spectroscopy (EDS), and electron backscatter diffraction (EBSD). The basic sample preparation steps included grinding with SiC papers of different grits (320, 800, 1200, and 2000), polishing with diamond suspensions of 3 μm (6 to 10 minutes) and 1 μm (20 minutes) and final polishing with SiO_2 suspension of 0.04 μm (40 minutes). For SEM and EDS analyses, the samples were electrolytically etched in a 10 pct aqueous solution of ammonium persulfate for 1.5 minutes and at 6 V potential. The used etchant highlights second-phase precipitates containing Ti, Cr, and W. The Scanning Electron Microscope used was a JEOL 6500FD equipped with a Thermo Fisher NSS EDS and Nordlys II EBSD detectors. The EBSD measurements were performed using a step size of 0.1 μm, with the Oxford *hkl* Channel 5 acquisition software. The data were post-processed with the software EDAX-TSL OIM Data Collections 7 and, prior to analysis, data clean-up was made according to the following steps: 1st) clean-up by Grain Confidence Index (CI) Standardization, with tolerance of 5.0, minimum size of 2 and multi-row 1, and 2nd) clean-up by Neighbor CI Correlation, with minimum CI equal to 0.10.

The ODS nanoparticles dispersed in the matrix of the steel in the as-received condition and annealed at 1573 K were characterized using a JEM-2200FS Transmission Electron Microscope (TEM) in the Department of Metallurgy at Gent University, Belgium. Sample preparation involved the following steps: (1) mechanical grinding of plates with initial dimensions of 10 × 10 × 0.5 mm^3 until a thickness of 100 μm was reached; (2) cutting of disks with 3 mm in diameter; and (3) electropolishing of the disks in solution of 4 pct perchloric acid and 96 pct ethanol, in order to further reduce the thickness of the disks and to make them transparent to the electron beam.

The volume fraction of second-phase constituents was determined using micrographs obtained with the SEM and the image analysis software *ImageJ*, according to the procedure described in the ASTM E1245-03 standard.[29] The size distribution of oxide nanoparticles was also estimated using the software *ImageJ*, but in this case, the measurements were not automatized, due to limited contrast between particles and the matrix in the bright-field electron micrographs. For the size estimation, the longest distance within a particle boundary observed in 2D was taken as the average length of the particle.

In order to have an indication of the effect of the heat treatments on mechanical properties, Vickers hardness measurements were made on the as-received and annealed samples. The applied load was 0.3 kgf using a Struers Durascan 70 microhardness device.

2. *Exposure to Low-Energy Deuterium Plasma and Thermal Desorption Spectroscopy*

Samples in the as-received state and annealed at 1573 K for 1 hour were exposed to low-energy deuterium plasma in the Nano-PSI facility, at the Dutch Institute for Fundamental Energy Research (DIFFER), Eindhoven/The Netherlands. The exposure was made in 2 batches; for each batch, a total of four samples with dimensions of 15 × 15 × 1 mm^3 were simultaneously exposed for 2 hours to the D_2 plasma with energy of 60 eV. The plasma energy derived almost entirely from a bias voltage of 60 V applied to the substrate holder. The plasma was mainly composed of D_3^+ ions; hence, each D atom impinging the samples had an energy of 20 eV. To minimize back-diffusion of D atoms from the sample, the backside of the samples was kept at room temperature during exposure. Figure 2(a) shows the spatial distribution of the ion flux and the electron temperature along a line through the center of the sample holder. Figure 2(b) is a schematic representation of the holder containing the four ODS 12 Cr samples during exposure to the D_2 plasma. The ion flux at the center of the holder (maximum in Figure 2(a)) was approximately 2.5 × 10^{20} m^{-2} s^{-1} resulting into a maximum ion fluence of 2.1 × 10^{24} m^{-2}.

After exposure, the samples were submitted to Thermal Desorption Spectroscopy (TDS), in order to determine the content of D retained in the steel and its trapping characteristics. One batch of samples was stored for 1 day at room temperature in a desiccator prior to the TDS measurement, another batch was stored for 25 days. In the TDS measurement, the samples were heated at a rate of 2 K s^{-1} from room temperature to 1200 K, which is the maximum temperature reached by the TDS. The initial pressure inside the TDS sample chamber was 3 × 10^{-7} mbar; however, when the system was at 1200 K, the pressure had increased to 10^{-5} mbar. The sample temperature was measured with a thermocouple welded to its surface and, to improve the thermal contact, graphite foils were inserted between the sample and the holder.

III. ANALYSIS AND MODELING OF THERMAL DESORPTION SPECTROSCOPY DATA

The D atoms introduced in the metallic microstructure during exposure to D_2 plasma can occupy normal lattice sites (interstitial positions) or trapping sites (defects). When located in a normal lattice site, the potential of the D atom is higher than at a trapping site, and hence, the latter forms a preferential site for D occupation. Both diffusion of D through the lattice and detrapping from a site require thermal activation. The activation energy for D diffusion through interstitial sites in α-Fe has been experimentally determined by Hagi and Hayashi[30] at 9 kJ mol^{-1} (0.09 eV), very similar to the activation energy for hydrogen diffusion (8 kJ mol^{-1}, 0.08 eV) and is considerably lower than the detrapping activation energy from trapping sites like dislocations, which has been determined by different authors to be 27 kJ mol^{-1} (0.28 eV).[30,31]

During a Thermal Desorption Spectroscopy measurement, the heating of a sample at a constant rate gradually provides the required thermal energy for the release of D atoms from the different sites. Each peak of maximum desorption rate in a TDS spectrum can be correlated with the release of D atoms from specific trapping sites in the material.[31,32] Several models have been developed to describe the diffusion and trapping behavior of hydrogen in metals,[33–35] which can be used to analyze TDS spectra and calculate kinetic parameters involved in hydrogen and deuterium evolution, especially when diffusion is the rate controlling process. For cases in which detrapping is the rate controlling process, the Kissinger theory of reaction kinetics[36,37] can be applied to TDS data, as first proposed by Choo and Lee[31] and later by Wei *et al.*[32,38,39] Wei *et al.*[32,38,39]

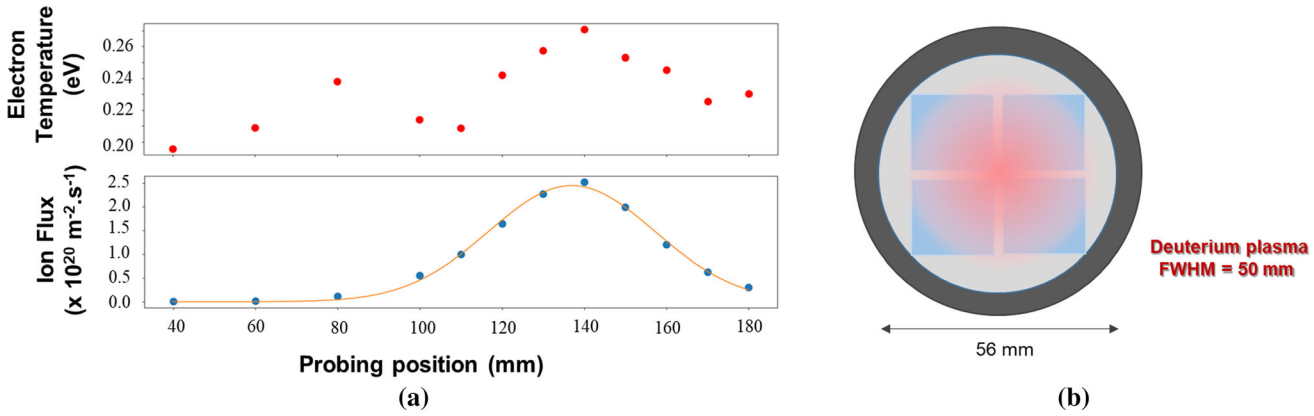

Fig. 2—(*a*) Parameters of D_2 plasma produced in the Nano-PSI at 2 SLM of the gas flow. (*b*) Schematic representation of the samples in the holder, exposed to D_2 plasma. The center of the holder receives the highest flux, and the decrease in color intensity represents the radial gradient of plasma fluence.

have shown that it is possible to obtain the activation energy for detrapping E_d by performing a numerical fit of the different maxima in a single TDS curve, using the Kissinger reaction rate equation:

$$\frac{dX}{dt} = A(1-X)^n \exp\left\{\frac{-E_d}{RT}\right\}, \quad [1]$$

where dX/dt is the release rate, A is a constant, X is the fraction of atoms released, n is the empirical reaction order, R is the gas constant, and T is the temperature. Originally, the constant A is known as the frequency factor and represents the probability of a molecule to participate in a chemical reaction.[37] When describing the detrapping-controlled desorption of hydrogen, Wei *et al.*[39] suggested that A approaches the pre-exponential factor p^0 in the McNabb and Foster theory[33,39]).

In the present work, an approach similar to the one of Wei *et al.* is used to estimate E_d of the different trapping sites present in the ODS 12 Cr steel. The fitting of the data is based on considering the experimentally measured TDS spectra to be the sum of several individual peaks. Each peak was modeled using a slightly modified version of Eq. [1], with $n = 1$ (*i.e.,* retrapping and diffusion are not considered[32,38,39]), given by

$$\frac{dN}{dt} = AN\exp\left\{\frac{-E_d}{kT}\right\}, \quad [2]$$

where dN/dt is the deuterium release rate in atoms s^{-1} and N is the number of D atoms in the trapping site. Since we report E_d in the unit eV, the Boltzmann constant k is used. The amount of D released in a time interval Δt is obtained by iteratively solving Eq. [2] with the initial condition $N(t = 0) = N_0$ and

$$N(t+\Delta t) - N(t) = \Delta t\left(\frac{dN}{dt}\right). \quad [3]$$

The initial value N_0 is treated as a fitting parameter.

The experimental heating rate of 2 K s^{-1} was introduced in the model by taking a temperature step of 0.2 K for every sufficiently small time step of 0.1 seconds.

IV. RESULTS AND DISCUSSION

A. *Characterization of the Microstructure After Different Annealing Treatments*

Figure 3 shows isopleths of the Fe–Cr equilibrium diagram for the ODS 12 Cr steel, calculated with Thermo-Calc v.2020a. For the Thermo-Calc calculations, the database used was TCFE10: "Steels/Fe alloys" and a simplified chemical composition of the ODS 12 Cr steel was inserted, in wt pct: Fe–0.03C–12Cr–1.7W–0.3Ti–0.144Y–0.05O. The Laves phase is a complex intermetallic that can form in the material after long exposures, of the order of thousands of hours, at intermediate temperatures.[40] Therefore, Laves Phase is not expected to be present in the

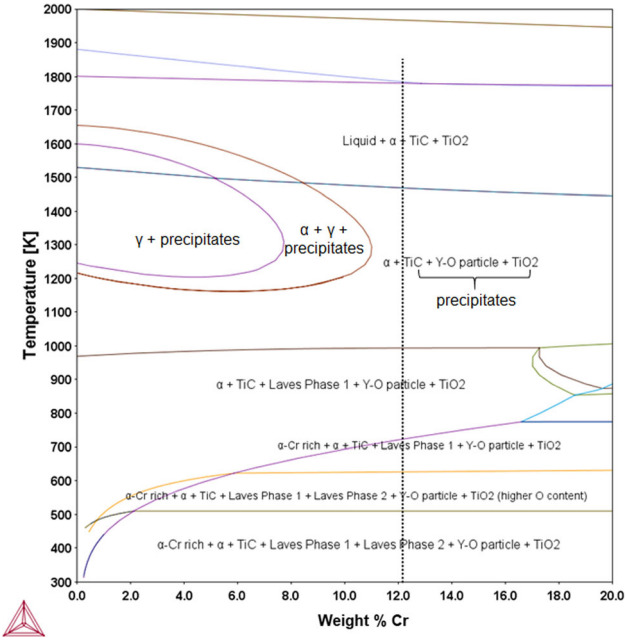

Fig. 3—Isopleths of Fe-Cr equilibrium diagram calculated with Thermo-Calc v. 2020a for the ODS 12 Cr steel. The dashed line marks the steels composition. For easier identification of γ loops, the termination precipitates are used to refer to TiC + Y–O particle and TiO_2.

as-received and annealed conditions of the ODS 12 Cr steel. TiO_2 is an oxide which could be present in the material but in practice is only found in ODS steels containing a minimum Ti content of 0.5 wt pct.[5,41] The Y-O particle indicated in Figure 3 corresponds to Y_2O_3. Thermo-Calc assumes that the oxide particles keep their original chemical composition (Y_2O_3) at all temperature ranges. Y_2O_3 can only be completely dissolved in steels during mechanical alloying and re-precipitates in the material during further heating stages, but with different chemical composition. The chemical composition of the re-precipitated Y–O-based nanoparticles depends on the alloying elements present in the steel. For the ODS 12 Cr steel, Ti is expected in the composition of its oxide nanoparticles.

Figures 4(a) and (b) presents low-magnification, backscattered electrons (BSE) micrographs of non-etched samples in the as-received condition and after annealing at 1573 K. The material contains pores formed during the fabrication process. Qualitatively, no increase in porosity and pore average size was observed with the increase annealing temperature for the 1 hour treatments. However, in Reference 42, an increase in the amount of pores and pore average size was reported for a very similar ODS steel annealed at 1573 K and 1673 K for 12 and 24 hours. Figures 4(c) and (d) shows higher magnification, secondary electrons (SE) micrographs of pores present in the ODS 12 Cr steel, annealed at 1573 K for 1 hour. Particles of a few hundreds of nanometers in size and spherical/cuboidal shape are found at the internal surfaces and interfaces of the pores. Samples in the as-received condition and annealed at lower temperatures also exhibit particles with these characteristics

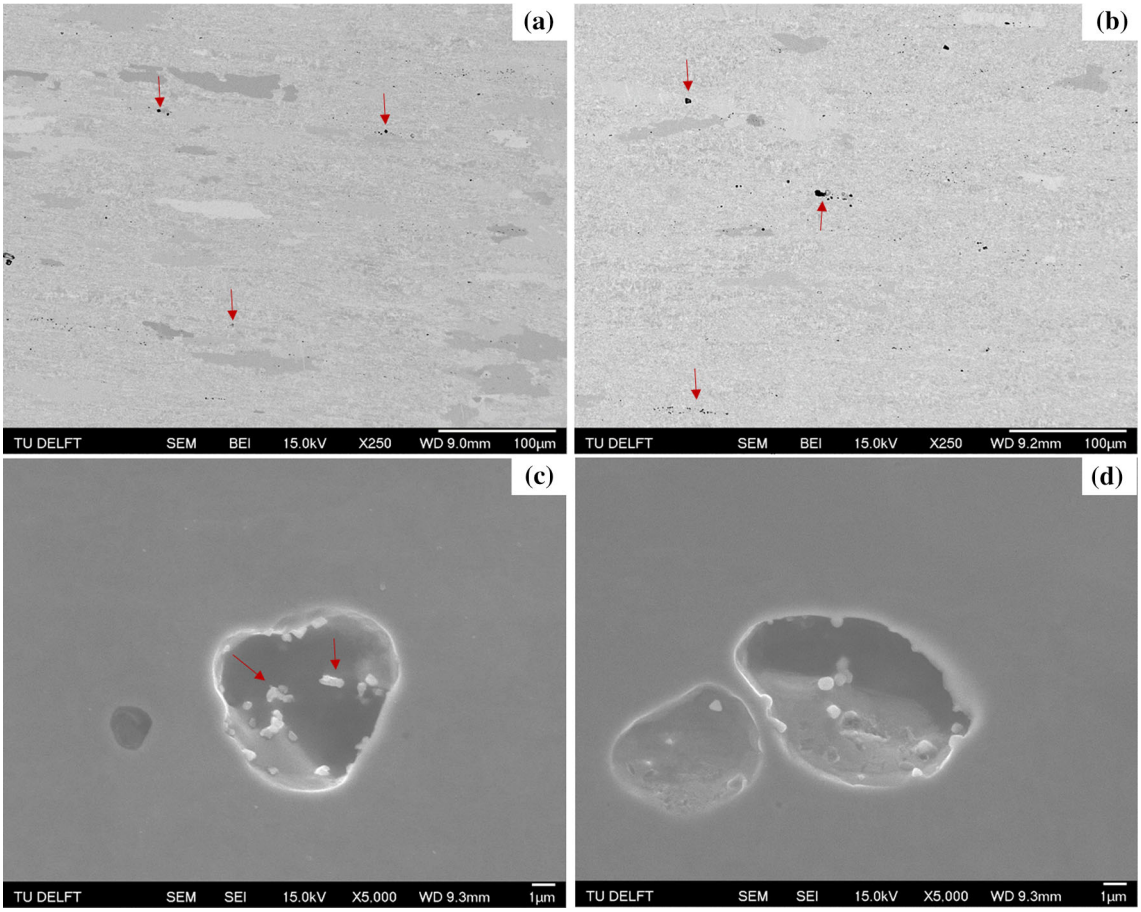

Fig. 4—Backscatter and Secondary Electrons micrographs of non-etched ODS 12 Cr steel in the (*a*) as-received condition, (*b*) annealed at 1573 K for 1 h, with red arrows indicating pores. In (*c*) and (*d*) a detailed view of pores, which contain particles (light gray) at their internal surfaces. The red arrows in (c) indicate groups of coalescing particles (Color figure online).

in some of their pores. In Figure 4(c), red arrows indicate groups of particles that likely have coalesced, with original particle boundaries still visible.

The estimated average diameter of the light-gray particles seen in Figures 4(c) and (d) is 0.5 ± 0.1 μm, the groups of particles indicated by the red arrows were counted separately, and their average length is $1.0 \pm 0.1\mu$m. EDS analyses were made on 27 of these light-gray particles encountered in the samples annealed at 1473 K and 1573 K. All results qualitatively indicate the presence of Y, Ti, and O in the particles. The EDS analyses of particles are considered qualitative due to (1) the size of the interaction volume of the electron beam with the material, which is larger than the analyzed particles, and (2) the fact that the particles are located inside pores. When the interaction volume of the electron beam with the material is larger than the particle size, the chemical composition of the matrix is also measured, influencing the resulting values. The curvature of the internal surfaces of pores on which the particles are located can also have a significant impact on electron scattering and also on the X-ray intensities measured, which can diverge considerably from their true chemical composition.[43] The emitted X-rays need to travel a certain length to reach the EDS detector and, when originating from regions of complex topology, they can be re-absorbed by the material.[43] A more precise determination of their chemical composition was made with the EDS system coupled to the Transmission Electron Microscope, and the results are given in Section IV–B.

Several authors[42,44–46] discussed the incorporation of Ar in ODS steels during mechanical alloying as the starting point for pore formation. In our discussion, we consider the concepts and evidence published by these authors, in order to clarify how pores can be produced in ODS steels and to explain the presence of coarse Y–Ti–O particles at internal surfaces of pores in our ODS 12 Cr steel. In Reference 46, micrometer-sized pores were observed in a 0.5 pct Y_2O_3-ODS 20 Cr alloy milled in hydrogen atmosphere, instead of Ar. The authors argue that pore formation is intrinsic to the mechanical alloying (MA) process, as they have found isolated pores in some of the MA powder particles, and that inert gas uptake during MA increases porosity in ODS steels.[46] So, besides dissolution of Y_2O_3 into Y and O, residual concentrations of Ar (or other gas) enter the metallic structure of the mechanically alloyed powders. Hence, at this stage, all elements are in solid solution within the Fe matrix, and some pores might be

already present in MA powder particles. When the MA powders are consolidated at high temperature (1100 K and above), either by hot isostatic pressing or hot extrusion, the oxide nanoparticles re-precipitate and the Ar atoms can

(i) diffuse through the lattice,
(ii) recombine with other Ar atoms and form bubbles, which can be located at grain boundaries or interfaces of second-phase particles, like carbides,[42,45]
(iii) stabilize vacancies either thermally formed[45] and/or induced by deformation, in the case of consolidation via hot extrusion and
(iv) accommodate and agglomerate at interfaces of oxide nanoparticles.[44]

Klimiankou *et al.*[44] have found nano-cavities filled with Ar at the interfaces of $Y_2Ti_2O_7$ nanoparticles in a 9 Cr ODS steel. In many cases, the authors observed multiple Ar nano-cavities trapped at the interface of a single oxide nanoparticle.[44] Ortega *et al.*[45] suggested that Ar atoms enable the nucleation of vacancy clusters in both non-ODS and ODS Eurofer steels. They provided evidence that Ar-vacancy clusters located in the matrix of steels and trapped at interfaces of Y–O nanoparticles are able to withstand high annealing temperatures and grow, forming larger defects (Ar-filled voids). Now, going back to the mechanism of pore formation and keeping in mind the results of References 44 and 45, we can infer that during thermo-mechanical treatment of the consolidated ODS 12 Cr steel, the initially small Ar bubbles and Ar-vacancy clusters, located either in the matrix or at interfaces of Y–Ti–O nanoparticles, are able to grow via Ostwald ripening and reach the micrometric dimensions observed in Figure 4. When pores are being formed at regions of the material with higher local density of oxide nanoparticles, the combination of (a) small inter-particle distance, (b) high temperature (1400 K and above), and (c) diffusion-assisted creation of surfaces inside newly grown pores, results in the local coarsening or coalescence of Y–Ti–O nanoparticles.

Figure 5 presents SE and BSE micrographs of the sample annealed at 773 K, etched with ammonium persulfate, which reveals micrometric precipitates. The black regions in Figure 5(b) correspond to pores. The precipitates are not homogeneously distributed throughout the sample and are aligned along the extrusion direction. In all analyzed samples, the precipitates have the same morphology and spatial distribution in the matrix. The chemical composition of the precipitates was determined with EDS and representative results are given in Figures 5(c) and (d). For all annealing conditions, the precipitates show a high EDS peak of Ti, and C is always detected. Peaks of Cr and Fe are also observed and, for precipitates smaller than 1 μm, their contents are close to the matrix composition (effect of size of interaction volume of the electron beam). Small contents of W (~ 2 wt pct) are detected in some of the particles. Hence, the precipitates correspond to TiC, in agreement with Thermo-Calc predictions. The equilibrium composition given by Thermo-Calc shows that the TiC should be formed by, in wt pct, 53Ti–46C–2Cr–2Fe–2W.

The volume fraction of TiC *vs* annealing temperature, determined with the software *ImageJ*, can be seen in Figure 6, along with the equilibrium molar fraction of TiC predicted with Thermo-Calc. The standard deviations associated to the measured average volume fractions are high, reflecting the heterogeneity of the precipitate distribution in the material. The average diameter of precipitates varies from 0.3 to 3 μm.

In general, the matrices of ODS steels are composed of micrometric grains surrounded by nanometric ones and, when chemically etched for SEM inspection, the regions containing nanometric grains are completely corroded, preventing a clear observation of grain boundaries. Hence, the use of orientation image maps (OIM) is a suitable option for the analysis of nanometric grains, since it does not require etching of samples. To adequately observe the ferritic matrix of the ODS 12 Cr steel, samples in the as-received state and annealed at 773 K, 1273 K, 1373 K, 1473 K, and 1573 K were analyzed with EBSD. Representative OIM are displayed in Figure 7, in which the gray-scale images correspond to Image Quality (IQ) maps and the colored ones are Inverse Pole Figure (IPF) maps. The elongation direction of the grains corresponds to the extrusion direction (indicated in Figure 7 as ED). Note that Figures 7(a) through (h) have different sample orientations inside the electron microscope. Figure 8 shows the grain size distributions of each analyzed sample, obtained by EBSD. The values of the *x*-axis correspond to the center of the bins, the bin size is 1 μm (TSL OIM software determines the lower boundary of the first size class as 0.15 μm).

Unlike the ODS Eurofer steel studied in Reference 47, the present material does not go through any phase transformation or substantial recrystallization. Thus, the microstructures in the as-received and annealed conditions are similar, composed of grains with 4 to 30 μm length and smaller ones with sizes of 0.2 to 4 μm. The IPF maps in Figure 7 qualitatively show that, for all conditions, the grains have a preferential orientation of $\langle 001 \rangle$ and $\langle 111 \rangle$ directions, which are in agreement with observations made on other ODS 12 Cr ferritic steels consolidated via hot extrusion.[2,6] In Reference 42, the authors detected substantial recrystallization only after 24 hours of annealing at 1573 K or 12 hours at 1673 K. The grain size distribution of Figure 8 displays information with sufficient statistical significance only of grains with sizes ranging between 0.15 and 6 μm—the number of larger grains is too small to determine the size distribution.

Figure 9 shows the Vickers hardness values of the ODS 12 Cr steel in all the analyzed conditions, along with data obtained previously for the ODS Eurofer steel in Reference 47. The latter presents hardness alterations that are in accordance with the microstructural processes taking place in the material (phase transformation and recrystallization), whereas the ODS 12 Cr steel exhibits constant Vickers hardness in almost the whole temperature range,

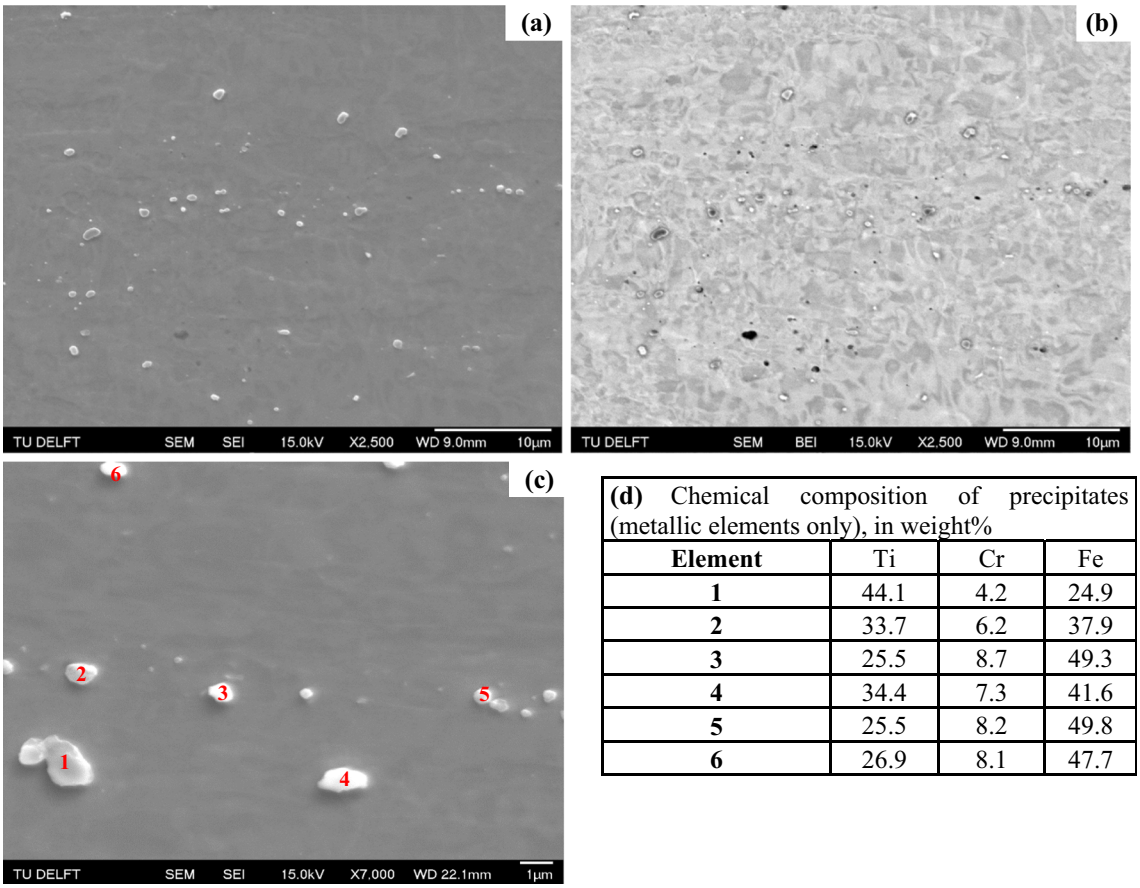

(d) Chemical composition of precipitates (metallic elements only), in weight%

Element	Ti	Cr	Fe
1	44.1	4.2	24.9
2	33.7	6.2	37.9
3	25.5	8.7	49.3
4	34.4	7.3	41.6
5	25.5	8.2	49.8
6	26.9	8.1	47.7

Fig. 5—(*a*) SE and (*b*) correspondent BSE micrographs of sample annealed at 773 K for 1 h, the red arrows indicate micrometric precipitates. (*c*) SE micrograph of precipitates present in the sample annealed at 1273 K and (*d*) contents of the main metallic elements present in the precipitates, determined with EDS (Color figure online).

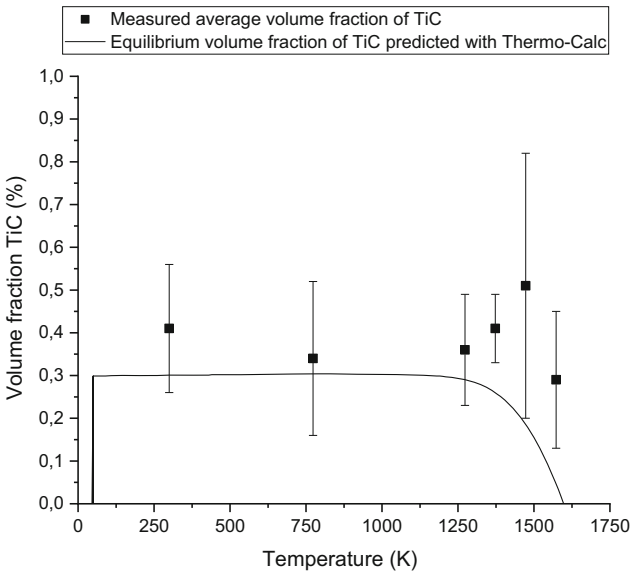

Fig. 6—Average volume fraction of TiC determined with *ImageJ* vs annealing temperature; the line corresponds to the equilibrium molar fraction of TiC predicted with Thermo-Calc v. 2020a, composition, and database used: Fe–0.03C–12Cr–1.7W–0.3Ti–0.144Y–0.05O and TCFE10: Steels/Fe alloys.

only going through a moderate decrease in hardness after annealing at 1573 K for 1 hour.

The results given in Figures 7 through 9 depict the high thermal stability of the ODS 12 Cr steel, which is in great part attributed to the addition of Ti in the material, known for refining the Y–O nanoparticles.[1,28] Thus, Y–Ti–O-based nanoparticles should remain refined even at temperatures as high as 1573 K and effectively prevent grain growth, due to a strong Zener pinning effect. Yet the moderate decrease in Vickers hardness after annealing at 1573 K signalizes the occurrence of a slight degree of softening in the material, not detectable in our microstructural analysis with SEM and EBSD. In the next section, we investigate the evolution of the oxide nanoparticles with temperature in more detail.

B. *Observation of Oxide Nanoparticles in the As-Received Condition and After Annealing at 1573 K*

In order to characterize the oxide nanoparticles present in the steel and investigate if they are altered after exposure to 1573 K, samples in this condition and in the as-received state were analyzed with Transmission Electron Microscopy (TEM).

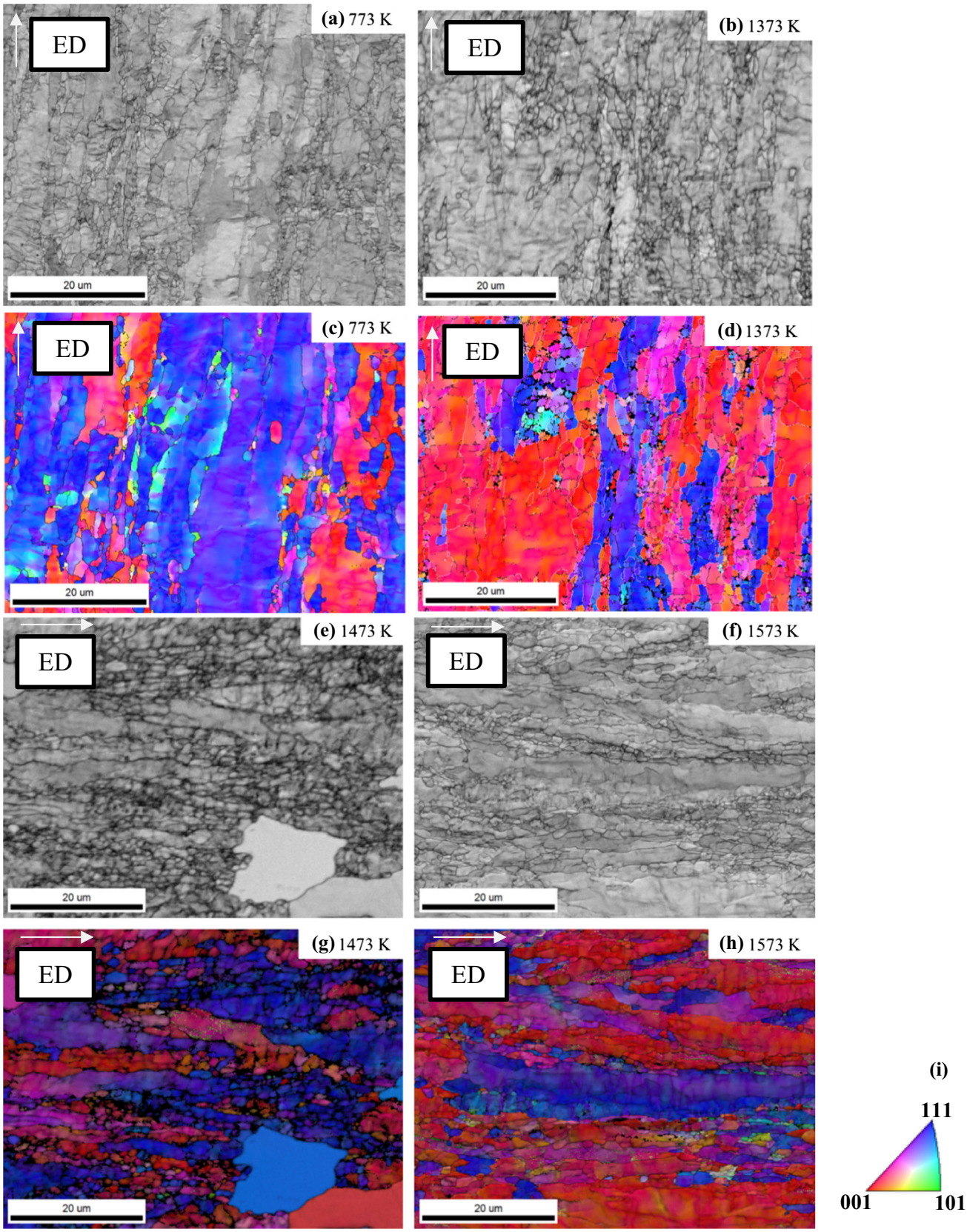

Fig. 7—Orientation image maps obtained with EBSD for the ODS 12 Cr steel after 1 h annealing at 773 K, 1373 K, 1473 K, and 1573 K. (*a*), (*b*), (*e*), and (*f*) are Image Quality maps; (*c*), (*d*), (*g*), and (*h*) are inverse pole figure maps; *i* color-coded map inverse pole figure (Color figure online).

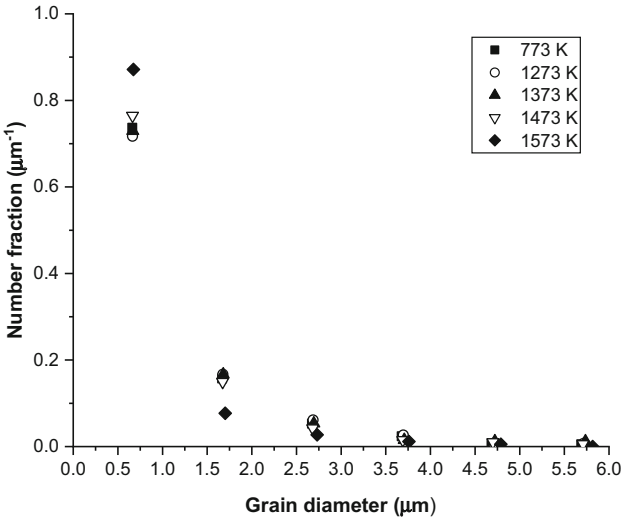

Fig. 8—Grain size distributions obtained with EBSD for the ODS 12 Cr steel annealed at different temperatures for 1 h.

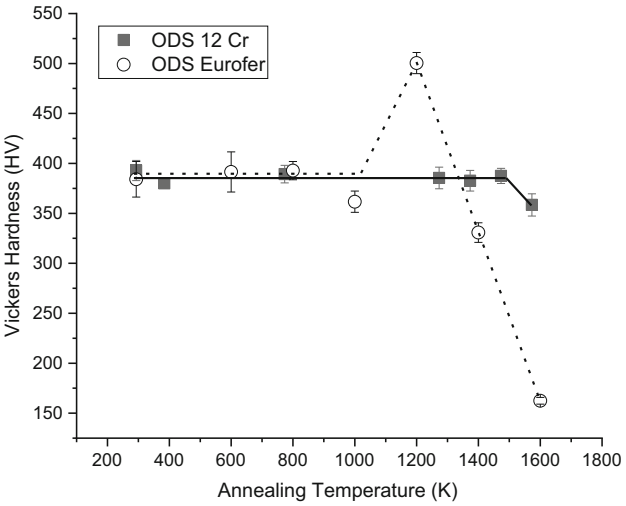

Fig. 9—Vickers hardness of the ODS 12 Cr annealed for 1 h at different temperatures, in comparison to the ODS Eurofer studied in Ref. [47].

Figure 10 presents bright-field micrographs of the material in the as-received condition, obtained in the STEM mode, and results of EDS measurements made on different features of the microstructure. Qualitatively, the material presents an expected high dislocation density, common in ODS steels due to severe deformation imposed during mechanical alloying and, in the case of the ODS 12 Cr steel, hot extrusion and other mechanical post-consolidation treatments. Figure 10(a1) corresponds to a detail of the indicated region in Figure 10(a). Nanosized particles are seen dispersed in the matrix, and some of them are pinning dislocations. Figure 10(b) shows a pore present in the as-received microstructure, which contains particles of 70 to 200 nm located at its interface. The results of EDS measurements given in Figure 10(d) show that the particles identified as 1 and 2 are Y–Ti–O based and particle 3 is TiC. These results confirm the observations made with SEM presented in Figure 4 and discussed in Section IV–A, of local coarsening of Y–Ti–O particles, due to enhanced diffusion at the internal surfaces and interfaces of pores. In Figure 10(c), with the exception of point 5 marked in the ferritic matrix of the steel, all points correspond to Y–Ti–O-based nanoparticles, with an estimated average particle size of 10 nm. In addition, in Figure 10(c), an outlined region containing Y–Ti–O particles with sizes ranging from 2 to 5 nm is displayed. The direct quantification of light elements like oxygen using EDS, whether in TEM or SEM, is complex. The X-ray peaks of oxygen and other light elements are located in the low-energy range of the EDS spectrum, subjected to the interference of the background radiation and of L, M, and N X-Rays emitted by heavier elements.[43] In the particular case of Cr-containing steels, the presence of Cr interferes with the detection of O, due to peaks of Cr-Lα with energy of 0.573 keV being close to the O-Kα 0.525 keV. Oxygen was detected in the present EDS analyses, but for the mentioned reasons, the O concentrations are not displayed in Figure 10(d).

Figure 11 contains bright-field micrographs of the sample annealed at 1573 K for 1 h, showing Y–Ti–O nanoparticles (Figures 11(a) and (b)), sub-micrometric particles inside a ferrite grain (Figure 11(c)), and results of EDS analysis (Figure 11(d)). The dislocation-free ferrite grain seen in Figure 11(c), which contains numerous sub-micrometric particles, is an indication that partial recrystallization is taking place in the material. Thus, the overall dislocation density in the annealed sample can be expected to be slightly lower than in the as-received condition. EDS analyses of the sub-micrometric particles in Figure 11(c) show that most of them are Y–Ti–O based. Still in Figure 11(c), red squares are indicating groups of particles undergoing coarsening: larger particles are growing, likely due to dissolution of smaller ones. Some of the coarse particles had a cuboidal shape, which is the most stable geometry of particles that are incoherent with the matrix. However, it is not clear why this pronounced coarsening occurs only locally in the material. A slight degree of recrystallization, accompanied by a decrease in dislocation density and local coarsening of Y–Ti–O particles to sub-micrometric dimensions, explains the moderate decrease in Vickers hardness measured after annealing at 1573 K for 1 hour.

Finally, the size distributions of the oxide nanoparticles present in the as-received and annealed conditions were calculated using bright-field images, and the results are displayed in Figure 12. The sub-micrometric particles, like the ones located at pores (Figure 10(b)) or the ones seen in Figure 11(c), were not taken into account. A total of 470 particles per condition were measured and, given that all had approximately spherical morphologies, the particle size was estimated to be the particle diameter.

The size distributions in Figure 12 show a clear coarsening of oxide nanoparticles during annealing at 1573 K for 1 hour. In the as-received condition, the average diameter of the particles is 3.87 $\pm$ 0.04 nm, and after the annealing treatment, the size distribution has become broader, with a pronounced increase in particles

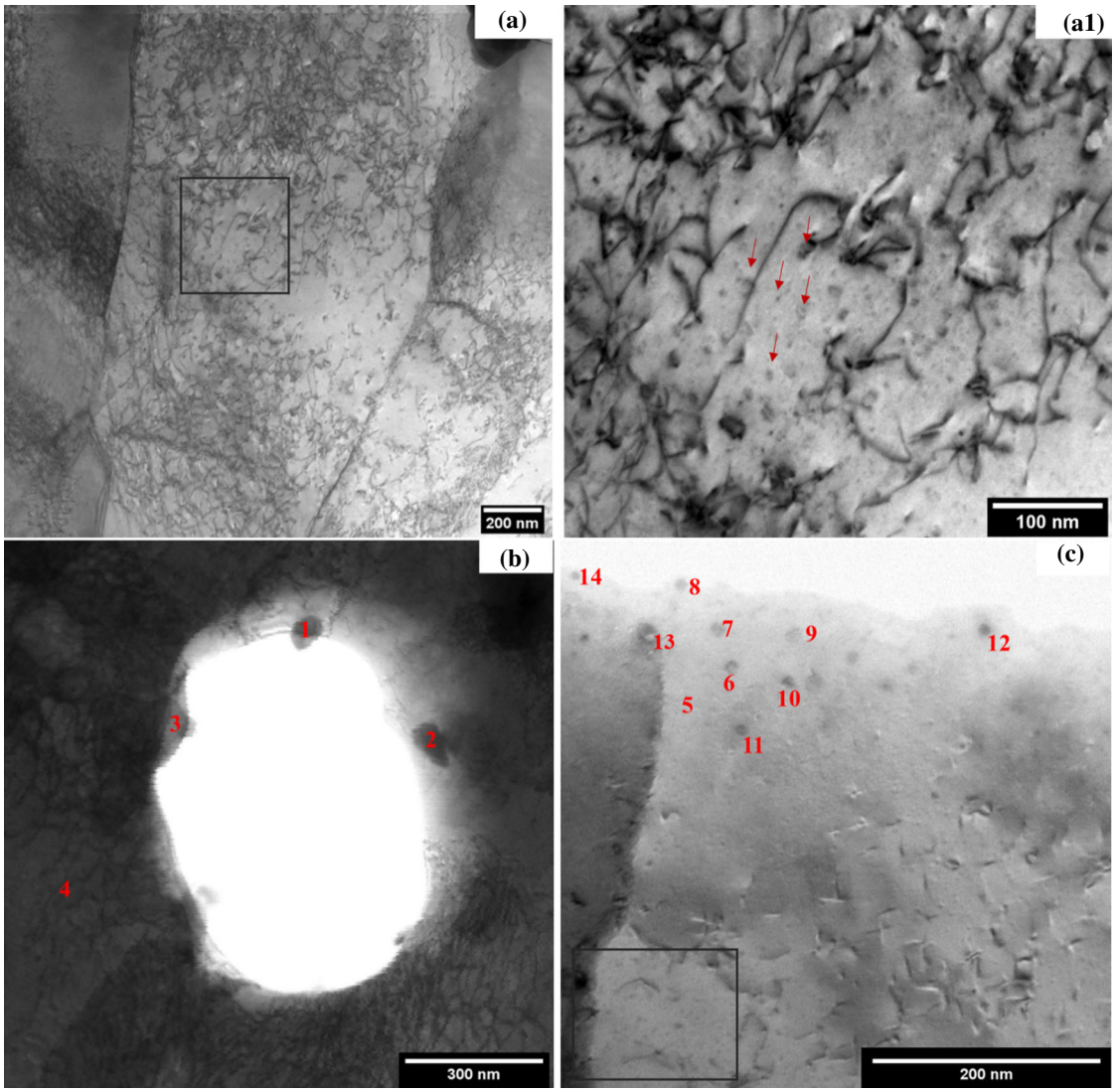

(d) Characteristics and chemical composition of point analysis indicated in (b) and (c)				
Type of particle and estimated size	**Main metallic elements, weight %**			
	Ti	Cr	Fe	Y
1. Y-Ti-O particle, 72 nm	15.2	4.5	26.9	40.8
2. Y-Ti-O particle, 102 nm	5.0	9.9	60.5	18.8
3. TiC, 208 nm	71.2	4.3	16.2	4.4
4. Ferritic Matrix	0.1	13.7	86.0	0
5. Ferritic Matrix	0.2	14.4	78.7	0
6-14. Y-Ti-O particles, average of estimated sizes 10 ± 3 nm	**Average weight % ± standard deviation**			
	9 ± 4	9 ± 2	48 ± 15	29 ± 12

Fig. 10—(*a* to *c*) Bright-field micrographs of the ODS 12 Cr steel in the as-received condition, (*d*) results of chemical analysis of points indicated in (b) and (c), along with particle size estimated with *ImageJ*, considering the particle size equal to the longest distances between the particles extremities.

with diameter ranging from 5 to 10 nm and an average diameter of 6.9 ± 0.2 nm. The particle sizes measured in the as-received sample are in agreement with observations made on other ODS ferritic steels that did not undergo high-temperature annealing.[4,6] Other authors have also observed the coarsening of Y–Ti–O-based nanoparticles after 1 h annealing at temperatures above 1500 K.[48–50] Dou *et al.*[4] measured the coherence of orthorhombic/hexagonal Y_2TiO_5 nanoparticles in ODS ferritic steels and found that particles with a diameter

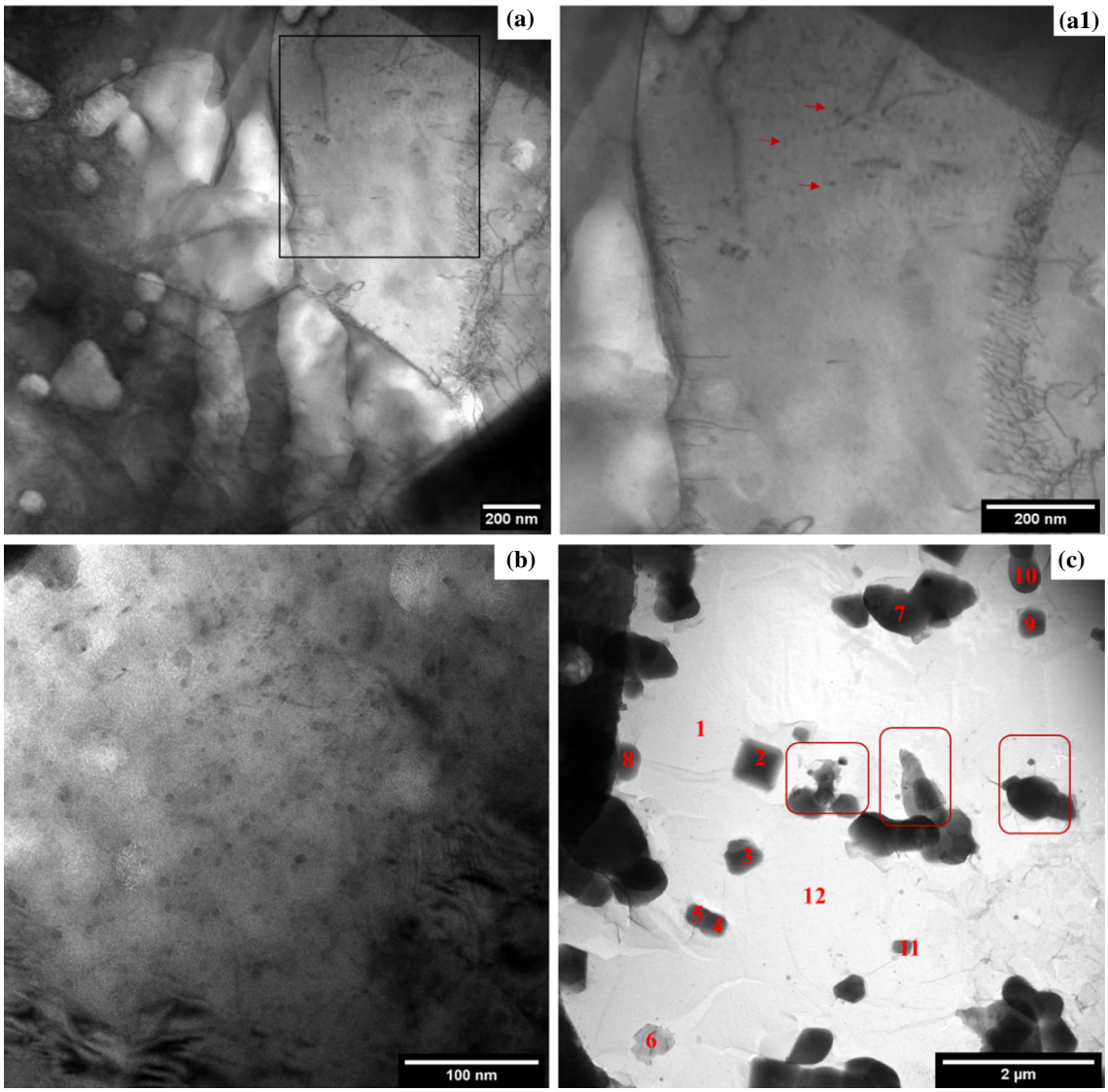

(d) Characteristics and chemical composition of point analysis indicated in (c)				
Type of particle and estimated size	**Main elements, weight %**			
	Ti	Cr	Fe	Y
1. Matrix	0.9	7.5	88.9	2.4
6. Matrix	0.8	11.0	87.9	0.2
8. Particle rich in Ti and Y	35.3	5.2	33.1	26.4
12. Matrix	2.4	11.4	83.1	3.1
2-5, 7, 9-11. Y-Ti-O coarse particles, estimated average size 490 ± 220 nm	**Average weight % ± standard deviation**			
	19.1 ± 1.5	2.5 ± 0.3	17.8 ± 1.3	60.5 ± 1.1

Fig. 11—(*a* to *c*) Bright-field micrographs of the ODS 12 Cr steel annealed at 1573 K for 1 h and (*d*) results of chemical analysis of points indicated in (c), along with particle size estimated with *ImageJ*, considering the particle size equal to the longest particle length.

smaller than 4.5 nm are coherent with the ferritic matrix, while particles with diameters between 4.5 and 10 nm are semi-coherent. Interestingly, the authors[4] also found that particles with a diameter larger than 10 nm are predominantly incoherent with the matrix. Thus, considering the tendency of Y–Ti–O nanoparticle coarsening shown in Figure 12, it can be assumed that the ODS 12 Cr steel annealed at 1573 K for 1 hour has a

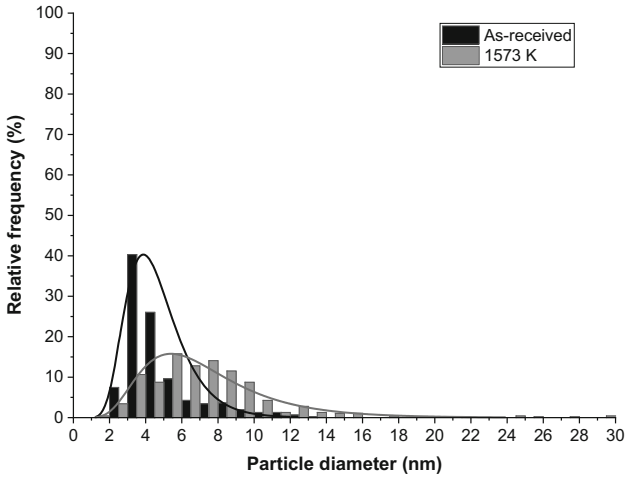

Fig. 12—Size distribution of Y–Ti–O particles present in the ODS 12 Cr steel on its as-received condition and after annealing at 1573 K for 1 h.

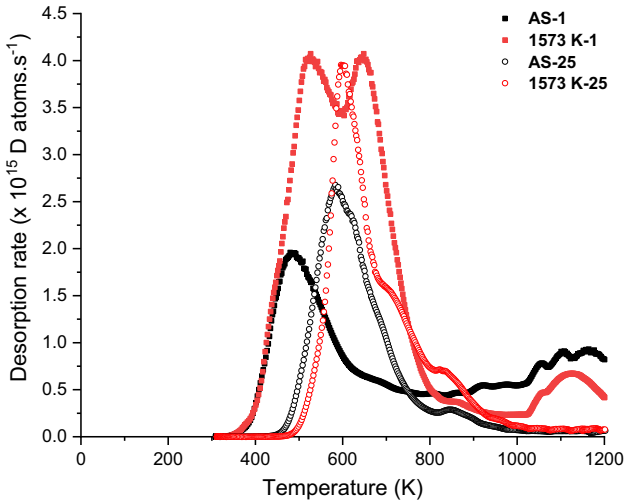

Fig. 13—TDS spectra measured on ODS 12 Cr steel samples in the as-received and annealed at 1573 K conditions. The samples were measured with TDS 1 day and 25 days after exposure to 60 eV D_2 plasma.

higher density of semi-coherent and incoherent nanoparticles than the as-received condition.

C. *Thermal Desorption Spectroscopy on Samples Exposed to Low-Energy D_2 Plasma*

The conditions selected for exposure to low-energy D_2 plasma and subsequent Thermal Desorption Spectroscopy were the as-received condition and annealed at 1573 K for 1 h. The main objective was to investigate the trapping behavior of deuterium in the material, particularly after the 1573 K annealing treatment, during which the coarsening of Y–Ti–O nanoparticles has occurred. In our previous work,[47] the thermal evolution of defects in an ODS Eurofer steel was studied with Positron Annihilation Spectroscopy Doppler Broadening. These results suggest that, during annealing at 1400 K and 1600 K, thermal vacancies become trapped at the interfaces of Y–O-based nanoparticles and, thus, retained in the microstructure after cooling to room temperature. The hypothesis raised in Reference 47 can be further explored in the present work.

Figure 13 presents the spectra of deuterium desorption rate *vs* temperature, obtained 1 day and 25 days after exposure to 60 eV D_2 plasma. The batch of samples measured 1 day after plasma exposure are named here as "AS-1 and 1573 K-1" and the batch measured 25 days after plasma exposure is referred to as "AS-25 and 1573 K-25." Table II summarizes the total amount of deuterium atoms released per sample, calculated by integrating the desorption curves.

The data presented in Figure 13 and Table II show that the samples annealed at 1573 K released more D than the samples in the as-received condition, by a factor of 2.0 after 1 day and a factor of 1.3 after 25 days. In addition, an effect of the waiting time prior to TDS can be seen, as samples measured 1 day after plasma exposure also released a higher number of D atoms than the ones measured 25 days after exposure, by a factor of 1.4 for the as-received condition and a factor of 2.1 for the annealed condition. First, the effect of waiting time will be explored.

1. *The effect of waiting time*

It is possible to estimate the time for D atoms to diffuse out of the samples, using the expression of diffusion length:

$$x = \sqrt{2Dt}, \qquad [4]$$

where x is the diffusion length, which is taken here as the half-thickness of the sample ($x = 0.75$ mm), D is the diffusion coefficient of D in the material, and t is the time for D atoms to diffuse to the exit surface of the sample.

The D atoms have to diffuse through a structure with a high density of defects (grain boundaries, dislocations, TiC, Y–Ti–O nanoparticles); thus, the value for D actually corresponds to an effective diffusion coefficient, D_{eff}. Esteban *et al.*,[25] using the gas permeation method, obtained the Arrhenius parameters for the effective diffusion of H in ODS Eurofer: $D_0 = 1.33 \times 10^{-6}$ m^2 s^{-1} and $E_{\text{dif}} = 30.4$ kJ.mol^{-1} (activation energy for diffusion). Since ODS 12 Cr and ODS Eurofer steels have a similar defect density and, as discussed previously, it is considered that H and D have the same behavior in steels, and we used the parameters determined by Reference 25 to calculate D_{eff} for D in the ODS 12 Cr steel at different temperatures. Finally, the D_{eff} values were used in Eq. [4] and the time for D atoms to diffuse out of the samples was obtained as a function of temperature. At room temperature (300 K), $D_{\text{eff}} = 6.8 \times 10^{-12}$ m^2 s^{-1} and $t = 41{,}500$ seconds, or 11.5 hours; at higher temperatures, t is reduced to tens of seconds, for example, at 600 K, t is 93 seconds and at 800 K, t is 20 seconds. Hence, even after 1 day, the samples may have already lost a fraction of mobile D prior to the TDS measurement, just by being kept at room temperature, confirming the release of D during

the waiting time of 25 days. This confirms the observed loss of D during the waiting time of 25 days.

In order to investigate in more details the release of D at 300 K, it is necessary to determine the activation energies for detrapping, E_d, associated to the desorption peaks.

Figures 14(a) and (b) shows the modeling of TDS spectra of the samples AS-1 and AS-25, done with the use of Eq. [2]. As stated before, Eq. [2] does not consider retrapping and assumes that diffusion of D is fast in comparison to the detrapping rate. In addition, when at the maximum of the desorption peak, the number of atoms of D still residing at the specific trapping site corresponds to 40 pct of its initial concentration N_0 ($0.4N_0$). Thus, by integration of Eq. [2], at a constant temperature, the time for reaching the state $N = 0.4N_0$ is given by

$$t_{40\text{pct},300\text{K}} = \frac{-\ln(0.4)}{A\exp\left(\frac{-E_d}{kT}\right)}. \quad [5]$$

The values of A, E_d, N_0, and $t_{40\text{pct},300\text{K}}$ are given in Table III.

The types of trapping sites present in samples AS-1 and AS-25 are expected to be the same, since the only difference between the two samples is the waiting time, at room temperature, to the TDS measurement. Therefore, the E_d values used in the modeling are equal for both samples. The amount of D atoms N_0 initially trapped at each type of defect is different, and only for the modeled peak at 450 K, the constant $A = 2.5 \times 10^4$ s^{-1}; for the others, $A = 10^4$ s^{-1}.

In Figure 14(a), the experimental spectrum AS-1 has a dominant desorption peak at 480 K, which cannot be modeled with a single spectrum. In order to reproduce its slope and overall shape, it is necessary to adopt an approach of multiple traps. The experimental peak at 480 K is, then, considered to be the result of desorption from different trapping sites with E_d 0.50 eV and 0.56 eV and peaks at 450 K, 480 K, and 535 K. The E_d and A values of the modeled peaks at 450 K and 480 K suggest that these two peaks occur because of the release of D from the same type of defect, but in a first stage at 450 K, desorption could be easier.[38] This choice of E_d and A for modeling the peaks at 450 K and 480 K is based on the number of defects detected during microstructural characterization: we aimed at consistency between modeling of TDS data and the microstructural observations. The only peak that was adequately modeled by a single spectrum was the one at 870 K in AS-25.

In Figure 14(b), the first desorption peak in the experimental spectrum of AS-25 is around 580 K, and the lower temperature peaks at 450 K, 480 K, and 535 K are absent, suggesting the depletion of these traps. The values of $t_{40\text{pct},300\text{K}}$ displayed in Table III confirm this suggestion, as these lower temperature peaks are the only ones that can become fully depleted after 25 days at 300 K. Thus, in the modeling of AS-25, N_0 for these trapping sites is zero. Additionally, the modeling of AS-25 shows the increase of N_0 for trapping sites with $E_d = 0.61$ eV, 0.68 eV and 0.74 eV, suggesting the redistribution of D from lower to higher E_d sites.

The desorption peaks at temperatures above 900 K in the AS-1 and 1573 K-1 experimental spectra were not modeled, as they are believed to be caused by an increase in background pressure.

The same analysis was made for the samples 1573 K-1 and 1573 K-25, and the results are given in Figure 15 and Table IV.

The same modeling parameters as used in AS-1 and AS-25 were applied to 1573 K-1, with the addition of an extra peak at 650 K, present in its experimental spectrum (Figure 15(a)). The peak at 650 K can be modeled with the combination of $E_d = 0.68$ eV and $A = 0.6 \times 10^{-4}$ s^{-1}. This choice suggests that the modeled peaks at 627 K and 650 K belong to the same type of defect, but with desorption occurring in two stages, similarly to the proposed for the modeled peaks at 450 K and 480 K in AS-1 and 1573 K-1.[38]

In Figure 15(b), the peaks associated to lower-E_d sites are again not present because of their depletion after the 25 days waiting time. Nevertheless, the D desorption behavior in sample 1573 K-25 is more complex and could not be modeled completely. The peak at 580 K in AS-25 is shifted to 600 K in 1573 K-25 and cannot be modeled with Eq. [2]. The remaining high-temperature peaks are also shifted in comparison to 1573 K-1, AS-1, and AS-25, but it was possible to model these by using the same E_d values as for the other conditions and altering the value of A. In order to estimate N_0 of the peak at 580 K to 600 K in 1573 K-25, the area of the modeled peaks was subtracted from the experimental 1573 K-25 spectrum. The result is $N_0 = 4 \times 10^{16}$ atoms, a value similar to the one in 1573 K-1, and an indication that redistribution of D from shallower traps to deeper ones does not occur. The N_0 value of the peak at 627 K to 650 K is also considerably lower in 1573 K-25, corresponding to 63 pct of N_0 of the same peaks in 1573 K-1.

2. *Effect of Annealing at 1573 K*

It is clear that the annealing treatment at 1573 K for 1 hour has an effect on the trapping and desorption behavior of D in the ODS 12 Cr steel, seen in Table II as the higher amount of D atoms released, the extra desorption peak at 650 K in 1573 K-1 and the change in the constant A used to partially model the 1573 K-25 spectrum. The Electron Microscopy analyses of the microstructure and of oxide nanoparticles discussed in Sections IV–A and IV–B show that the ODS 12 Cr steel contains of many different defects: ferrite grain boundaries, dislocations, micrometric TiC, coherent (particle size smaller than 4.5 nm), semi-coherent (particle size between 4.5 and 10 nm), and incoherent (particle size higher than 10 nm) Y–Ti–O nanoparticles, coarse Y–Ti–O-based particles (located at pores and with average size ranging from ~ 200 nm to 1 μm) and pores. The as-received microstructure is only altered after annealing at the high temperature 1573 K, when an increase in the average Y–Ti–O nanoparticle size to ~ 7 nm and partial recrystallization are observed. These microstructural alterations would imply an overall lower density of defects, but, nevertheless, the deuterium intake was higher.

Table II. Total Number of Deuterium Atoms Released from ODS 12 Cr Steel Samples at Different Conditions, 1 Day and 25 Days After Exposure to D_2 Plasma

	AS-1	1573 K-1	AS-25	1573 K-25
Deuterium Atoms Released	3.17×10^{17}	6.35×10^{17}	2.25×10^{17}	2.97×10^{17}

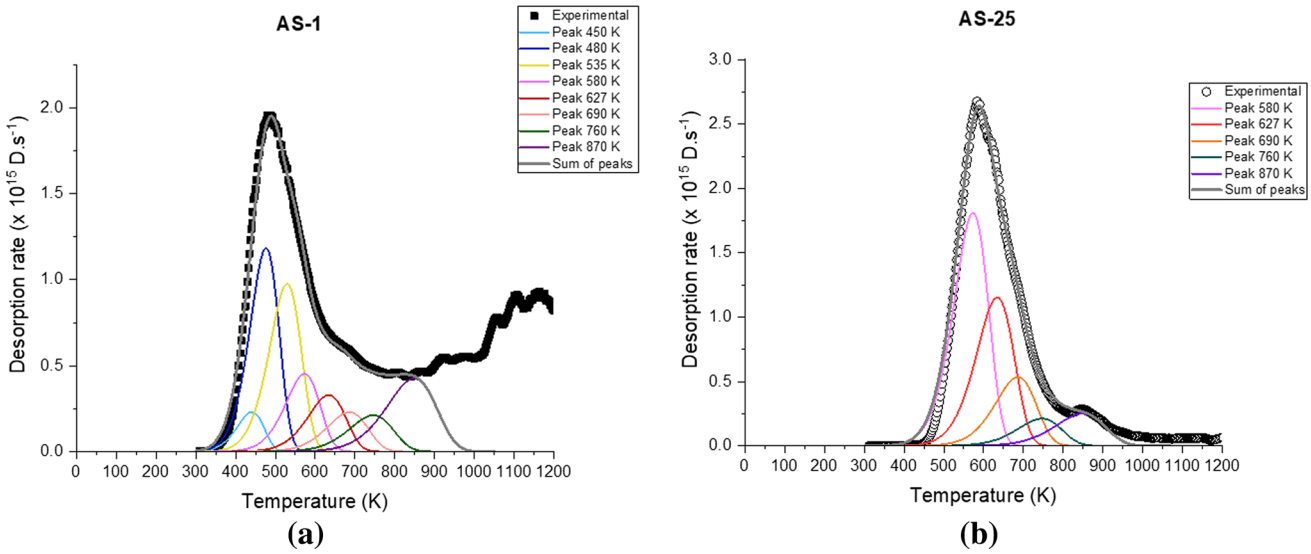

Fig. 14—Modeling of TDS spectra obtained for ODS 12 Cr steel samples (*a*) AS-1, measured 1 day after D_2 exposure and (*b*) AS-25, measured 25 days after exposure (Color figure online).

Table III. Parameters Used in the Modified Kissinger Equation (Eq. [2]) for Modeling TDS Spectra of ODS 12 Cr Steel in the As-received Condition and the Estimated Time for Depletion of Trapping Sites at 300 K

Peak Temperature (K)	E_d (eV)	A (10^4 s^{-1})	AS-1 N_0 (10^{16} D atoms)	AS-25 N_0 (10^{16} D atoms)	$t_{40pct,300K}$ (days)
450	0.50	2.5	1.0	0	0.1
480	0.50	1	5.5	0	0.3
535	0.56	1	5.0	0	3
580	0.61	1	2.5	10.0	19
627	0.68	1	2.0	7.0	282
690	0.74	1	1.7	3.5	2.9×10^3
760	0.81	1	1.5	1.5	43×10^3
870	0.93	1	3.5	2.0	4.5×10^6

Possible explanations for the higher deuterium intake by the samples in the annealed condition are (1) the more abundant semi-coherent and incoherent Y–Ti–O nanoparticles are able to trap more D atoms and (2) the annealing treatment at 1573 K leads to the trapping of thermal vacancies at the interfaces of the nanosized and the coarse Y–Ti–O particles, thereby increasing the content of trapped D.

Hypothesis (1) could explain the broad peak at 650 K in the TDS curve of 1573 K-1. As discussed in 4.3.1., this peak was modeled by a multiple trap approach, in which the peaks at 627 K and 650 K, both, have $E_d = 0.68$ eV. The N_0 value of these two peaks corresponds to 2×10^{17} atoms (Table IV), one order of magnitude higher than the N_0 of the modeled peak at 627 K in AS-1 (Table III) and, thus, could be associated with the higher fraction of semi-coherent/incoherent Y–Ti–O nanoparticles. However, hypothesis (1) cannot explain the experimental TDS spectrum of 1573 K-25. If hypothesis (1) was indeed valid, it would be possible to model all other high-temperature peaks in 1573 K-25 with the same E_d and A parameters us_{ed} in the other conditions, only changing their respective N_0 values. Instead, the required different A values in the modeling of 1573 K-25 signalizes modifications of the other high energy sites and likely a change in the desorption mode of D. Hence, hypothesis (2) could be the reason for this observed behavior. After exposure to plasma, D atoms

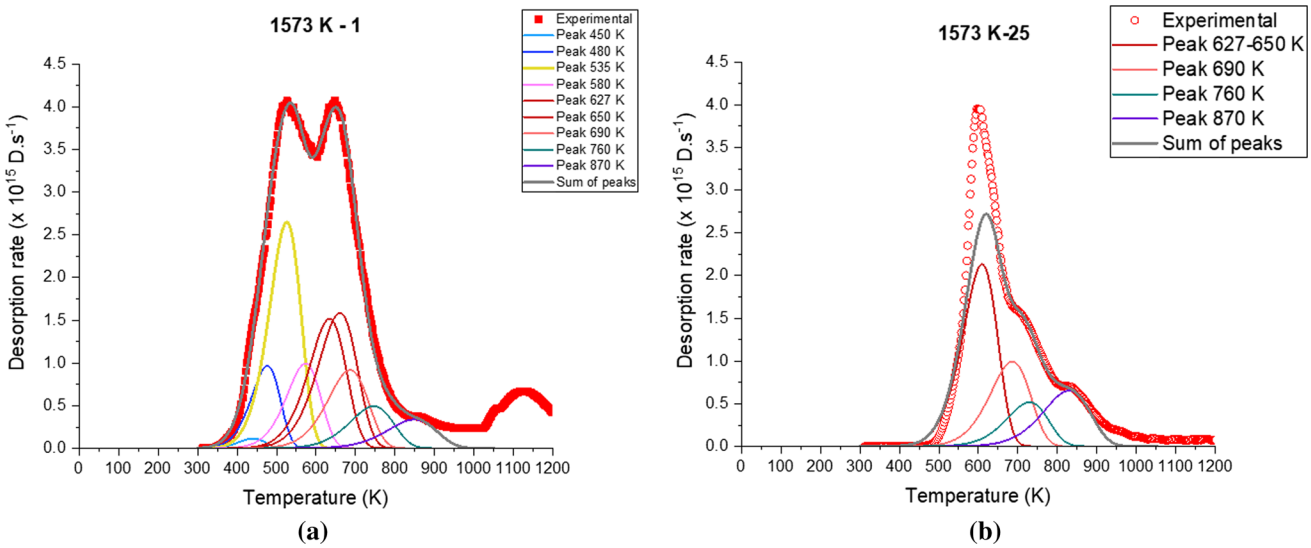

Fig. 15—Fitting of TDS spectra obtained for ODS 12 Cr steel samples (*a*) 1573 K-1, measured 1 day after D_2 exposure and (*b*) 1573 K-25, measured 25 days after exposure (Color figure online).

could be initially trapped both at the interface of the oxide/vacancy clusters and inside the vacancy clusters. When the size of the vacancy cluster is large enough, the trapped D atoms can form D_2 molecules, which will have a desorption mechanism different from the D^+ state. After the 25 days waiting time, most part of D would be trapped in the form of D_2, leading to the observed different desorption kinetics. According to Reference 12, first-principles' studies have shown that oxygen-vacancies complexes in Y–Ti–O nanoclusters are not able to trap a high number of hydrogen atoms, because the oxygen atoms absorb most of the charge density supplied by surrounding iron atoms.[12] This could also explain why the D redistribution described for AS-1 and AS-25 does not occur in 1573 K-1 and 1573 K-25. In case, hypothesis (2) is confirmed, the complexes of thermal vacancies and Y–Ti–O nanoparticles are able to trap more D than the particles alone, but they could have become saturated during exposure.

Because of the complexity of the microstructure, its high thermal stability (heat treatments do not lead to easily detectable microstructural alterations) and a limited TDS dataset, it is not possible to reliably determine to which type of defect each modeled desorption peak in Figures 14 and 15 correspond to, although there is a correspondence between the number of identified defects and the number of peaks necessary to model the experimental TDS spectra.

Additional TDS measurements done at different heating rates and first-principles' calculations are necessary to further explore hypothesis (2), related to the behavior of D in the ODS 12 Cr steel annealed at 1573 K, and to characterize completely the trapping sites present in the material.

3. *Evaluation of the modified kissinger method for modeling TDS data*

Finally, we used TMAP7 simulations[51,52] to evaluate the use of Eq. [2] and, particularly, the choice of A values for modeling the experimental TDS data. In the original Kissinger's theory, the constant A represents the probability of a molecule to participate in a chemical reaction.[37] Hence, in a desorption experiment, the constant A can be seen as the probability of a deuterium atom to be desorbed from a trapping site. For a desorption process governed by detrapping, A approaches the pre-exponential factor p^0[39] in the probability p of release from a trapping site to a lattice site.[33,39] In TMAP7, p^0 is determined as the Debye frequency υ_0 ($\sim 10^{13}$ s^{-1}).

In case, we take $A = \upsilon_0$ in Eq. [2], for modeling the peak at 450 K, for example, the corresponding E_d becomes 1.3 eV. A good mathematical correspondence with TMAP7 is obtained when we take $E_d = 1.3$ eV and the diffusion parameters D_0 and E_{dif} as, respectively, 2.1 m^2 s^{-1} and 0.1 eV. These values of D_0 and E_{dif} again represent a first order, detrapping-controlled desorption reaction. However, the very high value of E_d strongly disagrees with the disappearance after 25 days of the low-temperature desorption peaks observed in samples AS-25 and 1573 K-25. To investigate the effect of diffusion on the position of the desorption peaks, TMAP7 simulations were carried out using the lattice diffusion parameters of D in pure α-Fe[30] ($D_0 = 2 \times 10^{-7}$ m^2 s^{-1} and $E_{dif} = 0.1$ eV), the assumption of $A = \upsilon_0$, $E_d = 1.3$ eV, and lower E_d values listed in Table III, in order to reproduce AS-1. For $E_d = 1.3$ eV, the result is a peak at 850 K; for the lower E_d values, a peak with the same shape and slope as the experimental AS-1 is obtained, but shifted to 380 K.

Nevertheless, the TMAP7 simulations performed with different diffusivities show that Eq. [2] and our choice of A values much lower than the Debye frequency are appropriate to model the TDS experimental data obtained for the ODS 12 Cr steel. A possible underlying physical reason for A being smaller than υ_0 is the effect of the entropy in the activation free energy. However,

Table IV. Parameters Used in the Modified Kissinger Equation (Eq. [2]) for Fitting TDS Spectra of the ODS 12 Cr Steel in the Condition Annealed at 1573 K, Measured 1 Day (1573 K-1) and 25 Days (1573 K-25) After Exposure to D_2 Plasma

1573 K-1					1573 K-25			
Peak (K)	Temperature	A (10^4 s^{-1})	E_d (eV)	N_0 (10^{16} D Atoms)	Peak Temperature (K)	A (10^4 s^{-1})	E_d (eV)	N_0 (10^{16} D Atoms)
450		2.5	0.50	0.5	450	2.5	0.50	0
480		1	0.50	4.5	480	1	0.50	0
535		1	0.56	13.3	535	1	0.56	0
580		1	0.61	5.5	580	not fitted	not fitted	not fitted
627		1	0.68	9.2	627 to 650	1.8	0.68	12.0
650		0.6	0.68	10.0				
690		1	0.74	6.0	690	1	0.74	6.5
760		1	0.81	3.5	760	1	0.81	3.5
870		1	0.93	2.7	870	1.4	0.93	5.0

within the framework of the present study, it is not possible to quantify this effect.

V. CONCLUSIONS

The microstructural characterization of the ODS 12 Cr steel after 1 hour annealing treatments at different temperatures allow the following conclusions:

(i) The microstructure of the ODS 12 Cr steel is complex, formed by a variety of highly thermally stable components: a ferritic matrix composed of nanosized and micrometric grains, which has an intrinsic resistance to recrystallization due to its texture; incoherent TiC particles, even present after annealing at 1573 K for 1 hour and pores containing coarse Y–Ti–O-based particles, likely formed due to Ar retention during mechanical alloying and Y–Ti–O nanoparticles.

(ii) Only after annealing at 1573 K for 1 hour, a moderate decrease in Vickers hardness was observed in the ODS 12 Cr steel, from ~ 380 HV to ~ 350 HV. It was also possible to detect with TEM an increase in average diameter of Y–Ti–O nanoparticles from ~ 4 to ~ 7 nm, which was associated to partial recrystallization of the material and to the decrease in hardness.

(iii) In comparison to the ODS Eurofer steel studied in our previous work,[47] the microstructural stability of the ODS 12 Cr steel is highly superior, confirming the beneficial effect of Ti addition on oxide nanoparticle refinement and stability.

The subsequent exposure to low-energy D_2 plasma of samples in the as-received and annealed at 1573 K conditions, followed by TDS measurements show the following behavior of deuterium:

(iv) During the waiting time of 25 days, at 300 K, D atoms initially trapped at low-energy sites (E_d = 0.50, 0.56 and 0.61 eV) are detrapped. It was observed in the as-received condition that part of the detrapped D is released from the material and part of it is redistributed to higher energy trapping sites. For the annealed condition, we only find evidence of release of the detrapped D atoms, without occurrence of redistribution to higher energy trapping sites.

(v) Prior annealing at 1573 K for 1 h increases the D uptake during exposure to low-energy D_2 plasma. The reason for this behavior is still not completely clear, but the hypothesis is that, during annealing, thermal vacancies are trapped by the Y–Ti–O particles (nanoparticles and even the coarser ones). The complexes of thermal vacancies and Y–Ti–O-based particles are able to trap a higher number of D atoms, which can form D_2 molecules inside the vacancies. The fact that no redistribution of D during the waiting time is observed for the annealed condition implies that the complexes of thermal vacancies + Y–Ti–O particles become saturated with D after plasma exposure.

(vi) Additional TDS measurements at different heating rates and the use of first-principle calculations are necessary to properly characterize the trapping sites in the ODS 12 Cr steel and to further understand the D behavior in the annealed condition.

ACKNOWLEDGMENTS

This research was carried out under project number T16010e in the framework of the Partnership Program of the Materials innovation institute M2i (www.m2i.nl), supported by the Dutch government, and the Dutch Institute for Fundamental Energy Research (DIFFER) (www.differ.nl), which is part of the Netherlands Organization for Scientific Research (NWO) (www.nwo.nl). The present work has also been carried out within the framework of the EUROfusion Consortium and has received funding from the Euratom Research and Training programme 2014–2018 and 2019–2020,

under grant agreement n. 633053. The views and opinions expressed herein do not necessarily reflect those of the European Commission. The authors would like to thank Dr. Mercedes Hernandez Mayoral, from the Department of Technology, Division of Materials for Energy Interest, CIEMAT, Madrid, for the clarifying discussion regarding the Transmission Electron Microscopy results.

AUTHOR CONTRIBUTIONS

VMP: conceptualization, methodology, validation, formal analysis, investigation, resources, data curation, writing—original draft, writing—review and editing. S-CW: conceptualization, methodology, formal analysis, resources, writing—review and editing. TM: conceptualization, methodology, resources, writing—review and editing. HS: term, conceptualization, methodology, validation, formal analysis, investigation, resources, writing—review and editing, supervision. JS: term, conceptualization, validation, writing—review and editing, supervision, project administration.

CONFLICT OF INTEREST

The authors declare that they have no competing financial interests or personal relationships that could have appeared to influence the work reported in this paper.

OPEN ACCESS

REFERENCES

1. S. Ukai, M. Harada, H. Okada, M. Inoue, S. Nomura, S. Shikakura, K. Asabe, T. Nishida, and M. Fujiwara: *J. Nucl. Mater.*, 1993, vol. 204, pp. 65–73.
2. T. Narita, S. Ukai, B. Leng, S. Ohtsuka, and T. Kaito: *J. Nucl. Sci. Technol.*, 2013, vol. 50, pp. 314–20.
3. M. Praud, F. Mompiou, J. Malaplate, D. Caillard, J. Garnier, A. Steckmeyer, and B. Fournier: *J. Nucl. Mater.*, 2012, vol. 428, pp. 90–97.
4. P. Dou, A. Kimura, R. Kasada, T. Okuda, M. Inoue, S. Ukai, S. Ohnuki, T. Fujisawa, and F. Abe: *J. Nucl. Mater.*, 2013, vol. 442, pp. S95–S100.
5. E. Gil, N. Ordás, C. García-Rosales, and I. Iturriza: *Fusion Eng. Des.*, 2015, vols. 98–99, pp. 1973–77.
6. Y. Li, J. Shen, F. Li, H. Yang, S. Kano, Y. Matsukawa, Y. Satoh, H. Fu, H. Abe, and T. Muroga: *Mater. Sci. Eng. A*, 2016, vol. 654, pp. 203–12.
7. J. Shen, Y. Li, F. Li, H. Yang, Z. Zhao, S. Kano, Y. Matsukawa, Y. Satoh, and H. Abe: *Mater. Sci. Eng. A*, 2016, vol. 673, pp. 624–32.
8. M.A. Moghadasi, M. Nili-Ahmadabadi, F. Forghani, and H.S. Kim: *Sci. Rep.*, 2016, vol. 6, pp. 1–10.
9. D. Kumar, U. Prakash, V.V. Dabhade, K. Laha, and T. Sakthivel: *J. Mater. Eng. Perform.*, 2017, vol. 26, pp. 1817–24.
10. S. Seils, A. Kauffmann, F. Hinrichs, D. Schliephake, T. Boll, and M. Heilmaier: *Mater. Sci. Eng. A*, 2020, vol. 786, p. 139452.
11. N. Sallez, P. Donnadieu, E. Courtois-Manara, D. Chassaing, C. Kübel, F. Delabrouille, M. Blat-Yrieix, Y. de Carlan, and Y. Bréchet: *J. Mater. Sci.*, 2015, vol. 50, pp. 2202–17.
12. W. Xing, X.Q. Chen, P. Liu, X. Wang, P. Zhang, D. Li, and Y. Li: *Int. J. Hydrogen Energy*, 2014, vol. 39, pp. 18506–19.
13. J. Ribis, M.L. Lescoat, S.Y. Zhong, M.H. Mathon, and Y. De Carlan: *J. Nucl. Mater.*, 2013, vol. 442, pp. S101–05.
14. A. De Bremaecker: *J. Nucl. Mater.*, 2012, vol. 428, pp. 13–30.
15. J.-J. Huet: *Powder Metall.*, 1967, vol. 10, pp. 208–15.
16. S.J. Zinkle and G.S. Was: *Acta Mater.*, 2013, vol. 61, pp. 735–58.
17. G.S. Was: *Fundamentals of Radiation Materials Science: Metals and Alloys*, Springer, New York, 2007.
18. J. Knaster, A. Moeslang, and T. Muroga: *Nat. Phys.*, 2016, vol. 12, p. 424.
19. A. Möslang, E. Diegele, M. Klimiankou, R. Lässer, R. Lindau, E. Lucon, E. Materna-Morris, C. Petersen, R. Pippan, J.W. Rensman, M. Rieth, B. Van Der Schaaf, H.C. Schneider, and F. Tavassoli: *Nucl. Fusion*, 2005, vol. 45, pp. 649–55.
20. R.L. Klueh, D.S. Gelles, and M. Okada: *Reduced Activation Materials for Fusion Reactors*, ASTM International, West Conshohocken, 1990.
21. F. Wei and K. Tsuzaki:Hydrogen trapping phenomena in martensitic steels 13 in *Gaseous Hydrogen Embrittlement of Materials in Energy Technologies*, R.P. Gangloff and B.P. Somerday, eds., Woodhead Publishing Limited, Sawston, 2012, 1st ed..
22. E. Malitckii, Y. Yagodzinskyy, M. Ganchenkova, S. Binyukova, and H. Hänninen: *Fusion Eng. Des.*, 2013, vol. 88, pp. 2607–10.
23. E. Malitckii, Y. Yagodzinskyy, and H. Hänninen: *Fusion Eng. Des.*, 2015, vols. 98–99, pp. 2025–29.
24. I. Maroef, D.L. Olson, M. Eberhart, and G.R. Edwards: *Int. Mater. Rev.*, 2002, vol. 47, pp. 191–223.
25. G.A. Esteban, A. Peña, F. Legarda, and R. Lindau: *Fusion Eng. Des.*, 2007, vol. 82, pp. 2634–40.
26. O.V. Ogorodnikova, Z. Zhou, K. Sugiyama, M. Balden, Y. Gasparyan, and V. Efimov: *Nucl. Fusion*, 2017, vol. 57, pp. 1–12.
27. O.V. Ogorodnikova, Z. Zhou, K. Sugiyama, M. Balden, G. Pintsuk, Y. Gasparyan, and V. Efimov: *Nucl. Fusion*, 2017, vol. 57, pp. 1–9.
28. T. Muroga, T. Nagasaka, Y. Li, H. Abe, S. Ukai, A. Kimura, and T. Okuda: *Fusion Eng. Des.*, 2014, vol. 89, pp. 1717–22.
29. E1245-95, *Annu. B ASTM Stand.*, 1999, vol. **3**(2), pp. 1.
30. H. Hagi and Y. Hayashi: *Trans. Japan Inst. Met.*, 1987, vol. 28, pp. 368–74.
31. W.Y. Choo and J.Y. Lee: *Metall. Trans. A*, 1982, vol. 13A, pp. 135–40.
32. F.G. Wei, T. Hara, and K. Tsuzaki: *Metall. Mater. Trans. B*, 2004, vol. 35B, pp. 587–97.
33. A. McNabb and P. Foster: *Trans. Metall. Soc. AIME*, 1063, vol. **227**, pp. 618.
34. R.A. Oriani: *Acta Metall.*, 1970, vol. 18, pp. 147–57.
35. K. Ono and M. Meshii: *Acta Metall. Mater.*, 1992, vol. 40, pp. 1357–64.
36. H.E. Kissinger: *Anal. Chem.*, 1957, vol. 29, pp. 1702–06.
37. H.E. Kissinger: *J. Res. Natl. Bur. Stand.*, 1956, vol. 57, pp. 217–21.
38. F.G. Wei and K. Tsuzaki: *Metall. Mater. Trans. A Phys. Metall. Mater. Sci.*, 2006, vol. 37A, pp. 331–53.
39. F. Wei, M. Enomoto, and K. Tsuzaki: *Comput. Mater. Sci.*, 2012, vol. 51, pp. 322–30.

40. O. Prat, J. Garcia, D. Rojas, G. Sauthoff, and G. Inden: *Intermetallics*, 2013, vol. 32, pp. 362–72.
41. N. Baluc, J.L. Boutard, S.L. Dudarev, M. Rieth, J.B. Correia, B. Fournier, J. Henry, F. Legendre, T. Leguey, M. Lewandowska, R. Lindau, E. Marquis, A. Muñoz, B. Radiguet, and Z. Oksiuta: *J. Nucl. Mater*, 2011, vol. 417, pp. 149–53.
42. J. Shen, H. Yang, Y. Li, S. Kano, Y. Matsukawa, Y. Satoh, and H. Abe: *J. Alloys Compd.*, 2017, vol. 695, pp. 1946–55.
43. D.E. Newbury and N.W.M. Ritchie: *J. Mater. Sci.*, 2014, vol. 50, pp. 493–518.
44. M. Klimiankou, R. Lindau, and A. Möslang: *Micron*, 2005, vol. 36, pp. 1–8.
45. Y. Ortega, M.A. Monge, V. de Castro, A. Muñoz, T. Leguey, and R. Pareja: *J. Nucl. Mater.*, 2009, vols. 386–388 (C), pp. 462–65.
46. Y.L. Chen, A.R. Jones, and U. Miller: *Metall. Mater. Trans. A Phys. Metall. Mater. Sci.*, 2002, vol. 33A, pp. 2713–18.
47. V.S.M. Pereira, H. Schut, and J. Sietsma: *J. Nucl. Mater.*, 2020, vol. 540, p. 152398.
48. K. Dawson and G.J. Tatlock: *J. Nucl. Mater.*, 2014, vol. 444, pp. 252–60.
49. J. Ribis and Y. De Carlan: *Acta Mater.*, 2012, vol. 60, pp. 238–52.
50. M. Dade, J. Malaplate, J. Garnier, F. De Geuser, N. Lochet, and A. Deschamps: *J. Nucl. Mater.*, 2016, vol. 472, pp. 143–52.
51. G. R. Longhurst, *TMAP7 User Manual*, 2008.
52. G.M. Wright, M. Mayer, K. Ertl, G. De Saint-Aubin, and J. Rapp: *J. Nucl. Mater.*, 2011, vol. 415, pp. S636–40.